

pubs.acs.org/cm Article

$Ln_{10}S_{14}O$ (Ln = La, Pr, Nd, Sm) Oxysulfides: A Series of Direct n-Type Semiconductors

Brian A. Wuille Bille, Anna C. Kundmann, Frank E. Osterloh,* and Jesús M. Velázquez*



Cite This: Chem. Mater. 2022, 34, 7553-7562



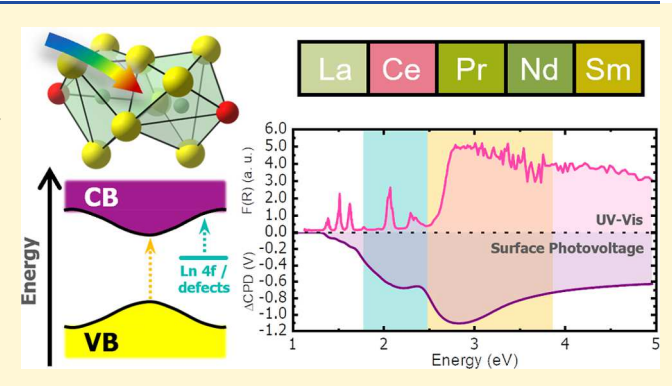
ACCESS I

III Metrics & More

Article Recommendations

s Supporting Information

ABSTRACT: Lanthanoid oxysulfides are promising materials for technological applications owing to their magnetic, photoluminescent, catalytic, and optoelectronic properties. Herein, we report the solid-state synthesis and structural characterization of $\rm Ln_{10}S_{14}O$ (Ln = La, Ce, Pr, Nd, Sm) oxysulfides. Then, we present a thorough discussion on their electronic and photophysical properties. Through Tauc plot analysis and the derivation of the absorption spectrum fitting method (DASF), we determine that all oxysulfides have direct band gaps with energies of 2.84 eV (La), 2.02 eV (Ce), 2.56 eV (Pr), 2.64 eV (Nd), and 2.41 eV (Sm). Furthermore, surface photovoltage spectroscopy (SPS) shows photovoltage (Δ CPD) values of -0.4 to -1.1 V for La-, Pr-, Nd-, and Sm-containing compounds when illuminated near the



optical band gap, indicating that these oxysulfides are n-type semiconductors, which is consistent with Mott–Schottky analysis. Photovoltages under sub-band gap illumination energy and photovoltage decay data suggest mid-band gap states possibly arising from the lanthanoid 4f orbitals and/or defects within the crystal structure or at the particle surfaces. These photophysical properties suggest possible applications of the oxysulfides in photoelectrochemical and photovoltaic energy conversion.

■ INTRODUCTION

The not-so-rare earths, i.e., lanthanoids, impart numerous electronic, magnetic, and optical properties to the compounds they form owing to their multiplicity of electronic energy levels, the presence of 4f orbitals, and high spin—orbit coupling. In the solid state, lanthanoid oxides have been the most widely studied materials, given their ease of synthesis, and industrial uses as supports for methane reforming, thermochemical fuel production, and photocatalysis. Sulfur substitution results in the narrowing of their band gaps to the visible region of the electromagnetic spectrum, relevant to applications as thermoelectrics, in solar energy conversion, and as nontoxic pigments. In Nevertheless, the band structure and optical absorption behavior of lanthanoid (oxy) sulfides are not yet well understood.

Initially misidentified as a lanthanoid sesquisulfide polymorph, β -Ln₂S₃, Ln₁₀S₁₄O represents a distinct tetragonal phase in which the oxygen atoms occupy the center of Ln(III) tetrahedra, surrounded by an intricate system of lanthanoid sulfide. In comparison to the oxysulfides of formula Ln₂O₂S, which have been studied for their optical properties as phosphors, language agents, and sulfur-tolerant catalysts, land comparatively less information is known of their higher sulfur content congeners, Ln₁₀S₁₄O. Having narrower band gaps as a result of the presence of quasistoichiometric sulfur, these oxysulfides have shown interesting photoluminescence and light absorption properties in

catalytic systems.¹⁷ However, much is yet unknown about their electronic structure, band gap energy, majority carrier type, and charge dynamics under illumination—factors relevant to optoelectronic applications of these compounds.

In this work, we study the structural and photophysical properties of Ln₁₀S₁₄O for the early lanthanoid ions La, Ce, Pr, Nd, and Sm. Specifically, diffuse reflectance UV—vis spectroscopy demonstrates that all oxysulfides possess band gap energies in the visible region of the electromagnetic spectrum. Moreover, through Tauc and derivation of the absorption spectrum fitting (DASF) analysis, it can be determined for the first time that the nature of the transition is direct. Finally, surface photovoltage spectroscopy (SPS) and Mott—Schottky plots show electrons to be the majority carriers in La₁₀S₁₄O, Pr₁₀S₁₄O, Nd₁₀S₁₄O, and Sm₁₀S₁₄O, allowing classification of these light absorbers as n-type semiconductors. Significant surface photovoltage generation under sub-band gap energy illumination suggests that defect states may be present in these compounds in addition to the participation of the Ln 4f

Received: April 25, 2022 Revised: July 22, 2022 Published: August 4, 2022





electrons. To the best of our knowledge, this work presents the first comprehensive study of the electronic and photophysical properties of these lanthanoid oxysulfides.

RESULTS AND DISCUSSION

Crystal Structure. Powder X-ray diffractograms of the series of light lanthanoid oxysulfides are presented in Figure 1c.

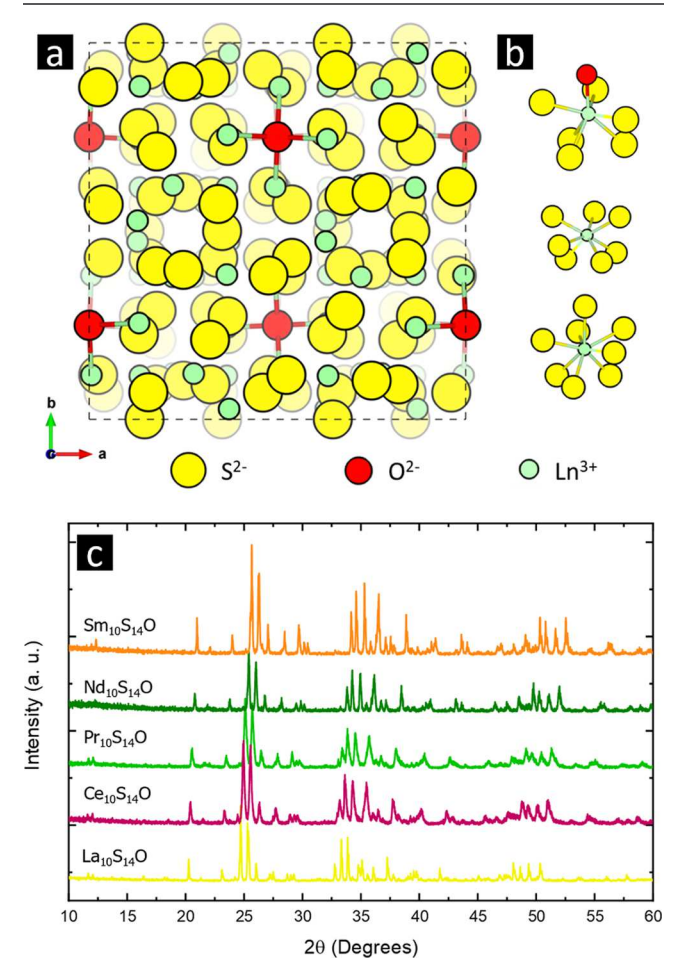


Figure 1. (a) Unit cell of $\mathrm{Ln_{10}S_{14}O}$ oxysulfides viewed along the *c*-axis, represented using the corresponding ionic radii in which the yellow, red, and green circles represent $\mathrm{S^{2-}}$, $\mathrm{O^{2-}}$, and $\mathrm{Ln^{3+}}$. (b) Structures highlighting the multiple 7- and 8-fold coordination environments surrounding the $\mathrm{Ln(III)}$ ions. (c) Powder X-ray diffractograms of the corresponding lanthanoid oxysulfides.

In a clear demonstration of the lanthanide contraction, a progressive shift to higher 2θ (or smaller d-spacing) of the characteristic reflections from their tetragonal unit cell ($I4_1/acd$ space group) can be observed with the increase in the atomic number. Following this trend, both the a and c lattice parameters show a decrease, as well as the anomalous c/a increase, in agreement with previous reports (Table S1). From the Rietveld refinements (Figure S1), the presence of secondary impurity phases can be identified. Such low levels of sulfide and oxysulfide phases tend to be present owing to the small region of stability known for the $Ln_10S_{14}O$ β structure in the $Ln_1OS_{14}O_xS_{1-x}$ structure destabilizes compared to Ln_2O_2S at high O contents. The $Ln_10S_{14}O$ unit cell is shown in Figure 1a,b. Therein, Ln^{3+} ions occupy three distinct crystallographic

sites: two sites of Wyckoff positions 32g and one 16f, exhibiting 7- and 8-fold coordination environments; the S^{2-} anions, sites 32g and 16e; and the O^{2-} the Wyckoff position 8a, in a tetrahedral configuration.

Consistent with the crystal structure, Ln L_3 -edge EXAFS results demonstrated a first coordination shell surrounding the Ln absorbers dominated by S^{2-} scatterers (Figure 2). At first,

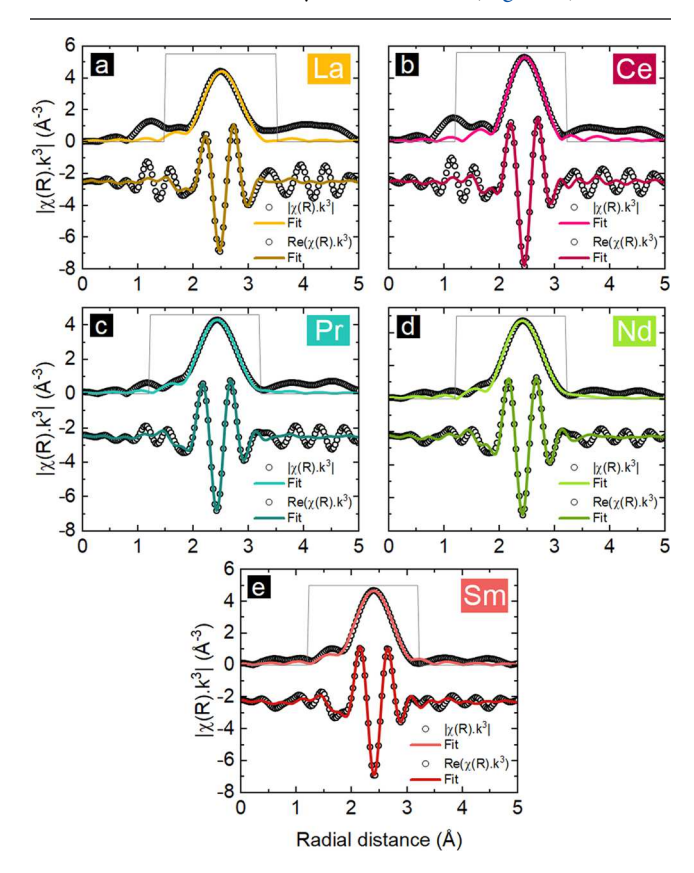


Figure 2. Nonphase-corrected lanthanoid L₃-edge FT-EXAFS fits for (a) La₁₀S₁₄O, (b) Ce₁₀S₁₄O, (c) Pr₁₀S₁₄O, (d) Nd₁₀S₁₄O, and (e) Sm₁₀S₁₄O. The top trace represents the magnitude of $\chi(R)\cdot k^3$, whereas the bottom constitutes its real component.

the lack of contribution of Ln–O scattering paths to the nearest-neighbors seemed peculiar, given its close distance (ca. 2.4 Å) in the coordination environment of the lanthanoid ions occupying one of the two 32g crystallographic sites. However, O^{2-} is only present in the immediacy of a single lanthanoid ion site and merely represents 1/7th of its neighboring ions. Thus, in the averaged data obtained for each sample, its contribution is significantly lower in comparison to that of the S^{2-} anions.

EXAFS analysis shows good agreement with crystallographic data and highlights the variety of Ln–S distances present surrounding each distinct lanthanoid crystallographic site (Tables S2 and S3) with a range of 2.919–3.027 Å for La, 2.839–2.967 Å for Ce, 2.838–2.983 Å for Pr, 2.746–3.053 Å for Nd, and 2.698–2.925 Å for Sm. Both Ln(III) ions occupying 32g sites, Ln1 and Ln2 (Figure S3), possess multiple nondegenerate S single scattering paths amounting to coordination numbers of 7, while the Ln(III) in 16f sites, Ln3, are characterized by multiple degenerate single scattering paths totaling an 8-fold coordination environment, which is more regular compared to the Ln1 and Ln2 sites. Considering a weighted average from the crystallographic data, the number of

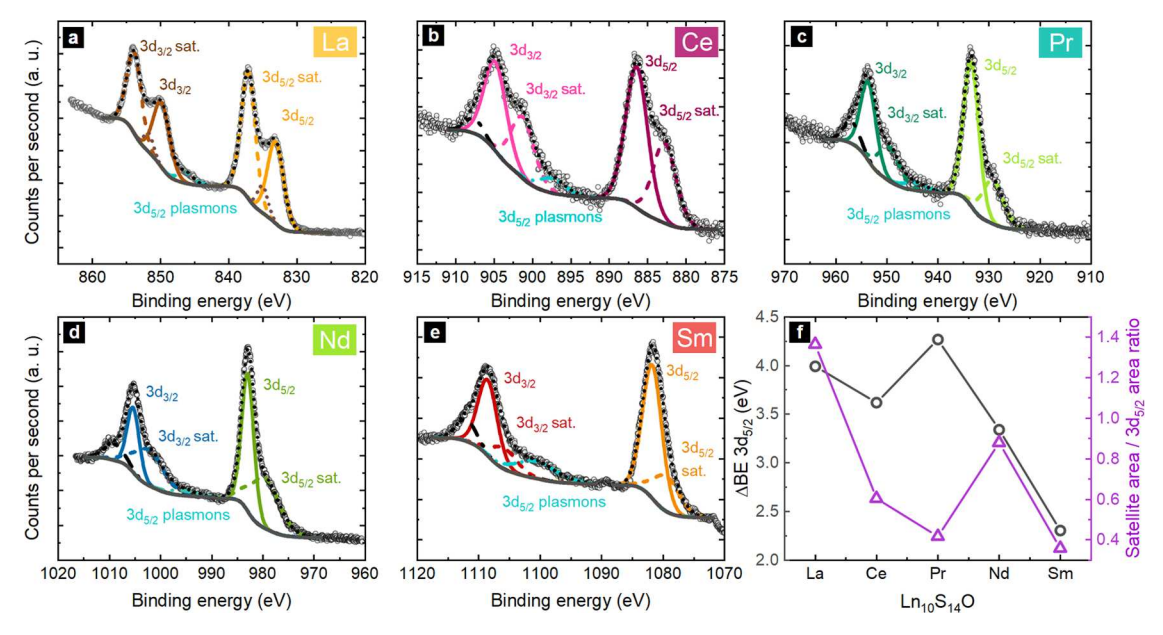


Figure 3. X-ray photoelectron spectroscopy of the Ln 3d region for (a) $La_{10}S14O$, (b) $Ce_{10}S_{14}O$, (c) $Pr_{10}S_{14}O$, (d) $Nd_{10}S_{14}O$, and (e) $Sm_{10}S_{14}O$. (f) Comparison between the binding energy difference and area ratio of the satellite-to- $3d_{5/2}$ signal as a function of the lanthanoid ion.

S atoms surrounding the lanthanoids corresponds to 6.8, which is consistent with the coordination number of 7 derived from the EXAFS fit. Interestingly, both Ln1 and Ln2 possess nearby second shell $\rm S^{2-}$ ions (ca ~3.4 Å) that contribute to the scattering signal observed.

Further structural information on these oxysulfides can be extracted through Raman spectroscopy. This technique is particularly useful given that in addition to band wavenumber position, the line shapes can inform on the degree of electronic or structural disorder.²² As seen in Figure S4a, the spectra for all lanthanoids show narrow bands indicative of an ordered structure amounting to fewer than 10 of the 93 predicted active modes for the point group $D_{4h}^{\ \ 21}$ In principle, an increase in the ionic radius would be expected to lead to a decrease in the wavenumber, due to longer bonds and smaller force constants, as observed in some Ln₂S₃ polymorphs.²³ This is the case for the vibrations in the range of 90-130 cm⁻¹. However, there is also the presence of bands that decrease their Raman shift with higher atomic number (ca. 82 and 140 cm⁻¹, Figure S4b). It is likely that the combination of increasing atomic weight and ionic character in going from La(III) to Sm(III) plays a role in the observed decrease of wavenumber.

Electronic Structure. The background-subtracted and normalized L_3 -edge X-ray absorption spectroscopy (XAS) spectra for all lanthanoids studied are provided in Figure S6. These transitions correspond to the dipole-allowed excitation of an electron from a core $2p_{3/2}$ orbital to empty states of 5d character (i.e., $2p^64f^95d^0 \rightarrow 2p^54f^95d^1$, where q corresponds to the number of f electrons in the ground state). Such spectra exhibit a characteristic sharp absorption. All Ln L_3 -edge energies are consistent with previous reports. Furthermore, the absence of multipeak white line features, caused by multiconfigurational ground states, indicates the absence of the Ln(IV) oxidation state in oxysulfides. Due to the $2p_{3/2}$ core—hole lifetime broadening, preedge features corresponding to the quadrupole transitions, $2p \rightarrow 4f$, were not detected in our XANES spectroscopy experiments and would require higher-resolution detection methods for their study.

Nevertheless, insight from the interaction of Ln 4f orbitals with those from the ligands can be gained from Ln 3d X-ray photoelectron spectroscopy (XPS) signals. As a result of spin orbit coupling, emitted 3d photoelectrons show two distinctive binding energy (BE) regions: $3d_{5/2}$ at a lower binding energy and $3d_{3/2}$ at a higher binding energy. Interestingly, all lanthanoids show an additional satellite signal of appreciable intensity. This has been attributed to the charge transfer from ligand valence orbitals to the core-ionized lanthanoid 4f. 28,29 In La₁₀S₁₄O, the higher binding energy peaks in both 3d_{5/2} and $3d_{3/2}$ regions correspond to the electron transfer satellite (Figure 3a). Unique to this close shell system (La³⁺), the satellite-to-3d signal ratio is greater than unity ($R_{\text{sat/3d}} = 1.33$). In the oxysulfide crystal structure, the coordination environment of the lanthanoid ions is dominated by S²⁻ anions; thus, this value is consistent with comparable soft ligands reported by Berthou and Jørgensen.³⁰ Conversely, in all of the remaining lanthanoids (Ce, Pr, Nd, and Sm), the charge transfer satellites appear at lower binding energies than the corresponding 3d signals (Figure 3b-e). This observation has been ascribed to an increase in stability of Ln^{3+} (3d 9 4f $^{q+1}$, after ligand charge transfer) relative to Ln⁴⁺ (3d⁹4f^q).³¹ Consequently, $R_{\text{sat/3d}}$ decreases with the increase in the effective nuclear charge along the period (Figure 3f), consistent with a decrease in the bond covalent character between the harder ${\rm Ln^{3+}}$ and the soft ${\rm S^{2-}}$ ligand. Importantly, the interpretation of the spectra for lanthanoids with multiple 4f electrons demands careful attention given the potential superposition of 3d⁹4f^q configurations with those corresponding to electron transfer final states 3d94fq+1. An expression of this multiplicity of states can be seen as the high binding energy $3d_{3/2}$ shoulders observed for Ce₁₀S₁₄O, Pr₁₀S₁₄O, Nd₁₀S₁₄O, and Sm₁₀S₁₄O.

Band Gap Determination. All $Ln_{10}S_{14}O$ display band gaps in the visible region of the electromagnetic spectrum as seen with the naked eye (Figure 4a). Upon sulfurization of the oxide precursors, the valence band becomes predominantly of S character, with its higher lying 3p orbitals, leading to narrower band gaps. ¹⁷ Diffuse reflectance UV–vis spectroscopy was used to probe the size (E_{σ}), as well as the type of band

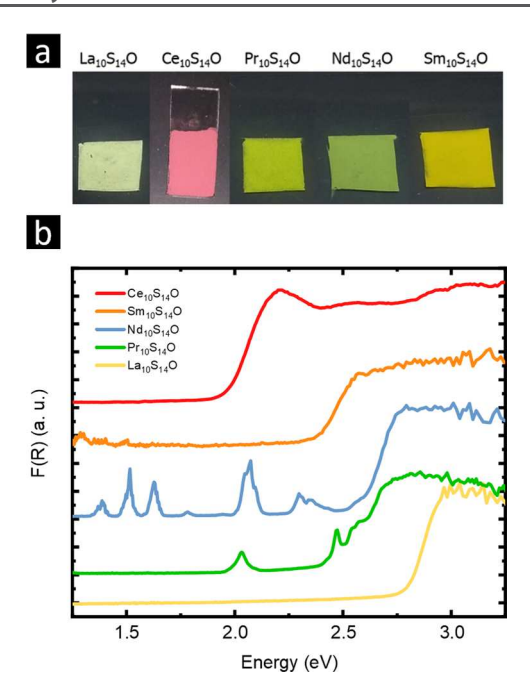


Figure 4. (a) Digital photographs of lanthanoid oxysulfide films on ITO substrates, and their (b) diffuse reflectance UV–vis spectra (shown offset for clarity). F(R) is proportional to the absorption coefficient. $F(R) = 2R/(1-R)^2$ (Kubelka–Munk function).

gap present, and the results are displayed in Figure 4. There is no direct monotonic trend in the $E_{\rm g}$ across the lanthanoid oxysulfide series. That is, Ce demonstrates a much narrower band gap than its predecessor, La; and Nd exhibits a wider band gap than Pr. In addition, Ln(III) f—f transitions are notable for Pr, Nd, and Sm. These are narrow absorption signals, which are largely unaffected by the chemical environment² but represent an additional challenge in the analysis of band gap type (*vide infra*) due to their overlap with the absorption edge.

The most widely used method for the determination of semiconductor band gaps is the Tauc plot analysis.³² This is based on the assumption that the absorption coefficient can be expressed as

$$(\alpha \cdot hv) = B(hv - E_g)^n \tag{1}$$

where h is the Planck constant, v is the photon frequency, E_g is the band gap energy, B is a constant, and n represents the nature of the transition. That is, n=2 for an indirect band gap, whereas n=1/2 for a direct transition. In diffuse reflectance measurements, the absorption coefficient α is approximated by the Kubelka–Munk function, F(R). By plotting $[F(R) \cdot hv]^{1/n}$ vs energy and extrapolating the linear absorption onset region to the abscissa, the band gap energy, E_g , can be estimated.

The use of the Tauc method inherently requires information on the nature of the transition, or an assumption of it *a priori*. Furthermore, it has been shown that its application to semiconductors with intraband gap absorption (caused by defects, doping, or surface/bulk modifications) can lead to inaccurate $E_{\rm g}$ estimations.³⁴ Thus, to aid in the distinction of the type of band gap, an orthogonal method for the analysis of reflectance spectra, known as the derivation of absorption spectrum fitting method (DASF),³⁵ was used. Through the calculation of the derivative of $\ln[F(R)/\lambda]$ with respect to $1/\lambda$, eq 2 is obtained.

$$\frac{\mathrm{d}\left\{\ln\left[\frac{F(R)}{\lambda}\right]\right\}}{\mathrm{d}\left(\frac{1}{\lambda}\right)} = \frac{n}{\left(\frac{1}{\lambda} - \frac{1}{\lambda_g}\right)} \tag{2}$$

Plotting the left side of eq 2 vs $1/\lambda$, the energy associated with the band gap can be determined from the peak maxima. The application of this method was especially important for the Ln₁₀S₁₄O oxysulfides studied given that both the indirect and direct band gap energies derived from Tauc analysis yield physically plausible values as shown in Table 1 and Figure 6.

Table 1. Band Gap Energies Obtained through Tauc and DASF Analysis and from SPS

	band gap (eV)			
material	Tauc indirect	Tauc direct	DASF	SPS
$La_{10}S_{14}O$	2.71 ± 0.05	2.84 ± 0.05	2.839 ± 0.002	2.5
$Ce_{10}S_{14}O$	1.88 ± 0.02	2.02 ± 0.02	1.996 ± 0.001	
$Pr_{10}S_{14}O$	2.36 ± 0.14	2.56 ± 0.11	2.566 ± 0.002	2.3
$Nd_{10}S_{14}O$	2.51 ± 0.08	2.64 ± 0.17	2.641 ± 0.003	2.4
$Sm_{10}S_{14}O$	2.23 ± 0.04	2.41 ± 0.04	2.442 ± 0.004	2.1

DASF and Tauc results show good agreement with a direct band gap for all oxysulfides. La $_{10}$ S $_{14}$ O, Ce $_{10}$ S $_{14}$ O, and Sm $_{10}$ S $_{14}$ O, exhibit sharp absorption onsets, leading to unequivocal DASF analysis (Figure 5c,f,o). On the other hand, both Pr $_{10}$ S $_{14}$ O and Nd $_{10}$ S $_{14}$ O spectra present a more challenging scenario due to the overlap with f–f transitions. In the Pr $_{10}$ S $_{14}$ O spectrum, three absorption bands corresponding to the excitations from the ground state 3 H $_4$ to the excited states 3 P $_2$ (2.57 eV, 482 nm), 3 P $_1$ (2.54 eV, 488 nm), and 3 P $_0$ (2.47 eV, 501 nm) can be clearly detected over the band gap absorption edge. Thus, the region used for the Tauc plot analyses corresponded to E > 2.57 eV (Figures 5g,h and 6).

The convolution of the f–f transitions with the band gap energy is further translated into the DASF analysis. Instead of a single peak, multiple maxima are present (Figure 5i,l). While this can certainly limit the value of this method, by increasing the user input in the process, if a judicious and consistent criterion is applied, we believe that useful information can be obtained and contrasted with that gained through the Tauc method. In our DASF analysis, we consider the highest energy maxima to be the band gap energies. Similar to the overlap observed in $Pr_{10}S_{14}O$, the $Nd_{10}S_{14}O$ reflectance spectrum shows a small shoulder, or Urbach tail, ca. 2.58 eV, which is likely caused by two f–f transitions: ${}^4I_{9/2} \rightarrow {}^4G_{11/2}$ (2.58 eV, 479.9 nm) and ${}^4I_{9/2} \rightarrow {}^2D_{3/2}$ (2.56 eV, 483.9 nm).

Photophysical Characterization. To probe the ability of the materials to generate mobile charge carriers under illumination, surface photovoltage spectroscopy (SPS) was employed. In SPS, a semitransparent vibrating Kelvin probe is used for the measurement of photoinduced charge transfer in particle films upon exposure to light of variable wavelength. The spectra of the particle films on fluorine-doped tin oxide (FTO) are presented in Figure S8 and are plotted alongside the optical absorption spectra in Figure 7. La, Pr, Nd, and Sm oxysulfides exhibit negative photovoltage (Δ CPD), indicating the transfer of electrons away from the Kelvin probe and toward the FTO substrate.

This confirms electrons as majority carriers and identifies the compounds as n-type semiconductors. This also agrees with the Mott–Schottky analysis of the semiconductor films in 0.1

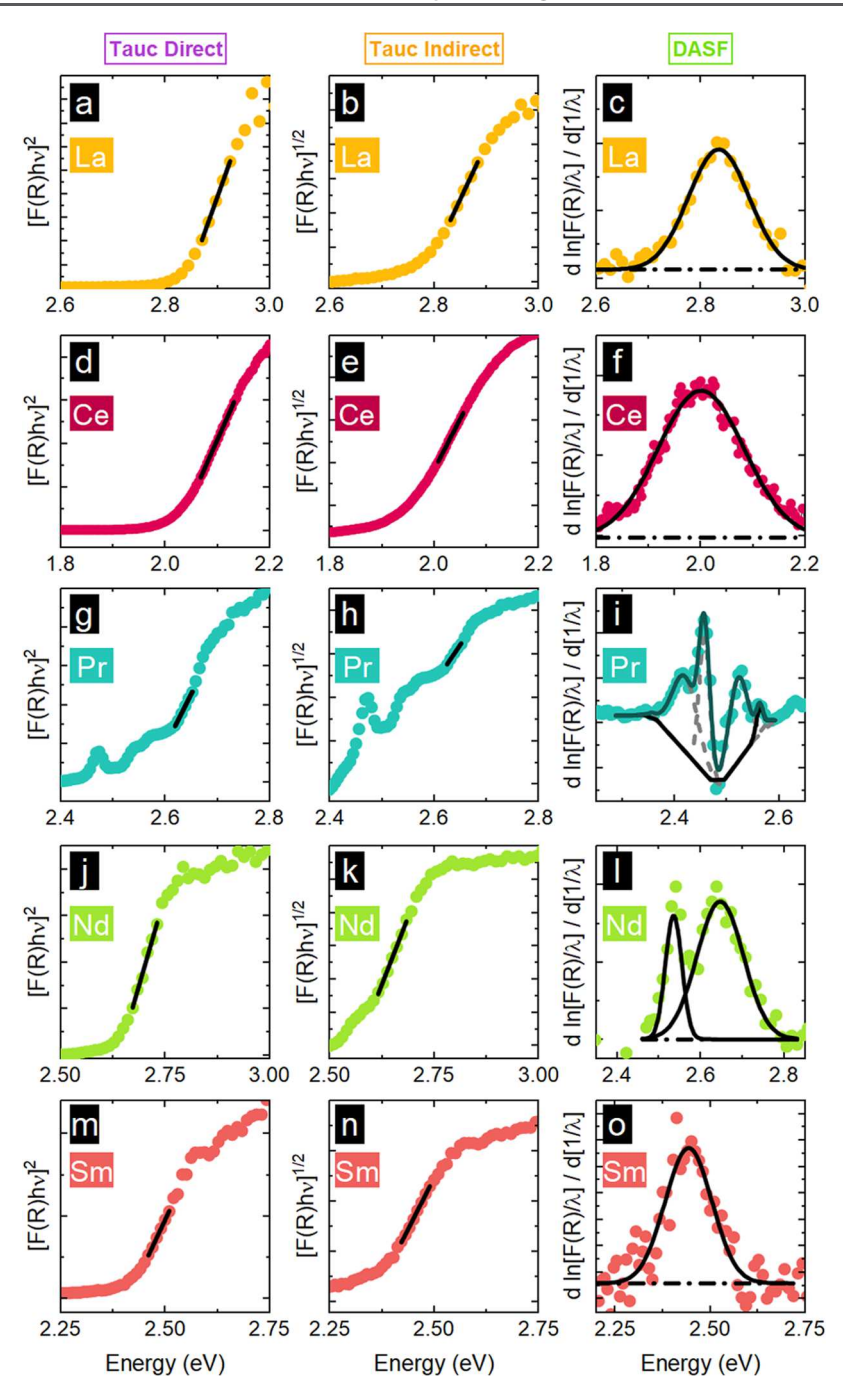


Figure 5. Comparison between Tauc direct, indirect, and DASF analyses for the determination of the optical band gap. The solid and dashed black lines represent linear regressions for Tauc analyses (left and middle columns) and Gaussian peak fittings for DASF analysis (right column).

M Na₂SO₄ (Figure S11). The photovoltage spectra resemble the optical spectra in that the major photovoltage signal occurs near the optical band gaps of the materials. This photovoltage is due to the separation of photogenerated charge carriers in the valence and conduction bands as shown in Figure 8c. As Table 1 shows, the effective band gaps from the spectra compare reasonably well with the direct band gaps from the DASF analysis. Additionally, all SPS spectra contain strong photovoltage signals at photon energies below the band gap. This is attributed to excitation and transfer of charge carriers in sub-band gap states (Figure 8c). Sub-band gap photovoltage signals from lattice defects are commonly found in SPS data due to the high sensitivity of the technique.^{39–41} In

chalcogenides, defects arise from cation vacancies, antisites, and chalcogen vacancies. $^{42-44}$ In oxysulfides, the defects are most likely sulfur vacancies that are caused by post-synthetic surface oxidation. Alternatively, it is possible that defect states are generated by cation disorder, 43 induced by the high heating and cooling rates (44 °C/min and 50 °C/min, respectively) during preparation. Lastly, lanthanoid 4f orbitals in conjunction with oxygen vacancies may create mid-band gap donor states. 45 This would explain the comparatively weaker "pre-edge" photovoltage observed for La₁₀S₁₄O, which is lacking 4f electrons. In this case, any sub-band gap photovoltage would have to arise from antisite defects or anion vacancies. Impurities may also play a role in the observed sub-

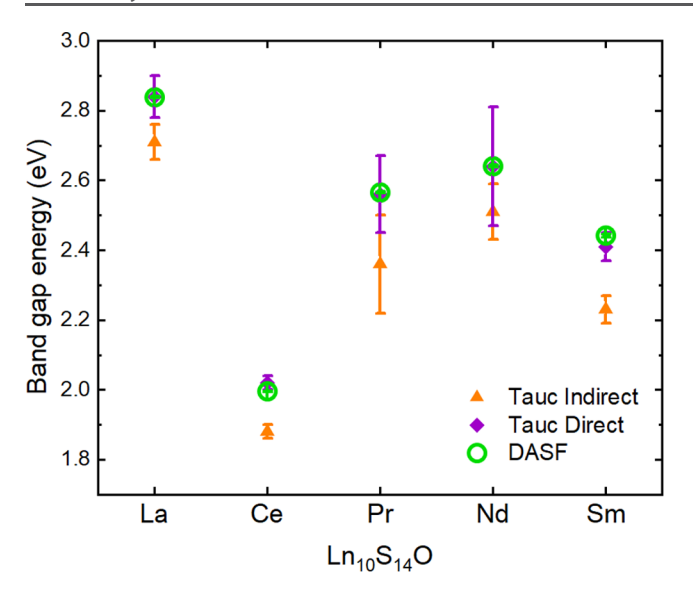


Figure 6. Comparison of band gap energy values obtained through Tauc plot and DASF analysis.

band gap photovoltage; however, the $\rm Ln_2O_2S$ impurity seen in Figure S1 possesses wider band gaps than the $\rm Ln_{10}S_{14}O$ phases.

To further characterize the photophysical properties of lanthanoid oxysulfides, surface photovoltage decay data following 400 nm (12.5 mW cm⁻²) illumination was recorded (Figure 8a). This provides information about the dynamics of charge carrier separation and recombination.^{47–49} For all tested oxysulfides, photovoltage signals form on the 10–20 s timescale (Figure 8a), reaching a final value comparable to that seen in the spectra in Figure 7. When the light is switched off,

the photovoltage decays asymptotically but does not quite reach zero over the duration of the experiment. La₁₀S₁₄O and Sm₁₀S₁₄O exhibit faster relaxation dynamics, with only 5.37 and 8.07% of the $\Delta \text{CPD}_{\text{max}}$ remaining after 27 min in the dark, while Pr₁₀S₁₄O and Nd₁₀S₁₄O retain 19.0 and 26.2% of their ΔCPD_{max} values (Table S5). The long timescale of the photovoltage decay suggests that recombination occurs by a thermally activated process. Here, electrons need to overcome an energy barrier before they can combine with a trapped photohole at the semiconductor surface. Peter et al. previously used the exponential function (eq 3) to model transient recombination photocurrents in photoelectrodes. 50,51 The model assumes that majority carrier transfer into surface states is limited by a potential barrier at the photoelectrode surface as shown in Figure 8d.⁵² By plotting $\ln[\Delta \text{CPD}(t)/\Delta \text{CPD}(t=0)]$ versus time (eq 4), the lifetime τ of the trapped minority carriers can be obtained from the slope of the linear graph.

$$\frac{\Delta \text{CPD}(t)}{\Delta \text{CPD}(t=0)} = e^{-t/\tau}$$
(3)

$$\ln\left[\frac{\Delta \text{CPD}}{\Delta \text{CPD}(t=0)}\right] = -\frac{t}{\tau} \tag{4}$$

From Figure 8b, it can be seen that this model captures the recombination kinetics of the $Ln_{10}S_{14}O$ phases at long times (t > 800 s) based on the linearity of the plots. This suggests that carrier recombination in $Ln_{10}S_{14}O$ films is indeed limited by processes at the particle surfaces. At shorter times, additional, faster recombination pathways are active, possibly involving the mid-band gap states discussed above. Based on the linear fits in Figure 8b, minority carrier lifetimes in surface states range from 934.6 s $(La_{10}S_{14}O)$ to 4098 s $(Nd_{10}S_{14}O)$ with the remaining two phases having intermediate τ values (Table S6

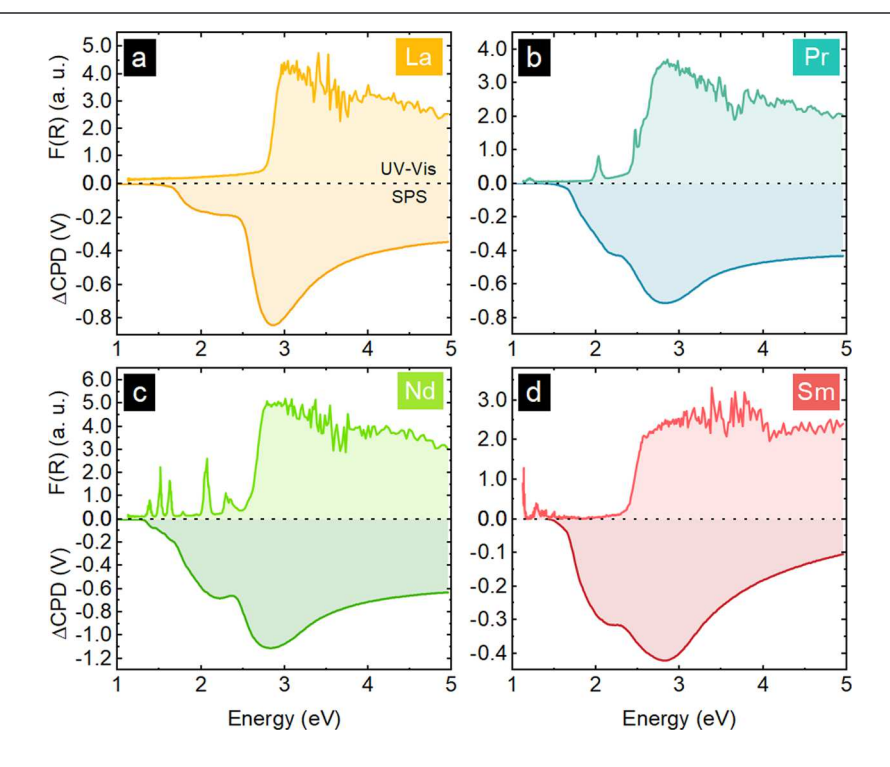


Figure 7. Comparison between DR UV-vis (top) and surface photovoltage spectra (bottom) of (a) $La_{10}S_{14}O$, (b) $Pr_{10}S_{14}O$, (c) $Nd_{10}S_{14}O$, and (d) $Sm_{10}S_{14}O$ films on fluorine-doped tin oxide (FTO)-coated glass slides in vacuum. Δ CPD is the contact potential difference versus the dark CPD value. For details, see the Experimental Section. Films of $Ce_{10}S_{14}O$ did not produce any photovoltage signal (Figure S9).

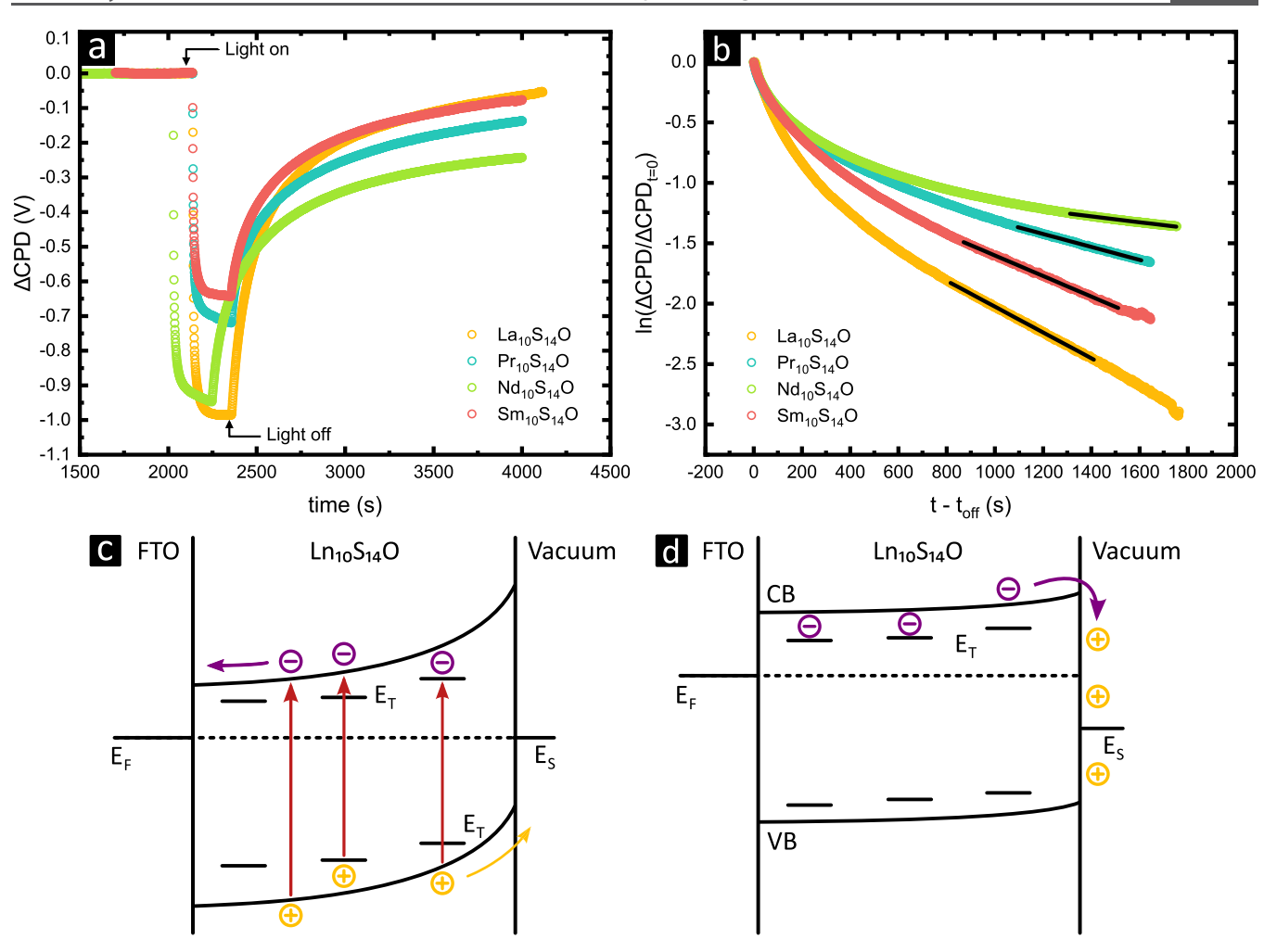


Figure 8. Photovoltage decay data of $La_{10}S_{14}O$, $Pr_{10}S_{14}O$, $Nd_{10}S_{14}O$, and $Sm_{10}S_{14}O$. (a) Δ CPD as a function of time, indicating the illumination period; (b) logarithmic plot of the normalized Δ CPD decay, and straight lines indicate linear regressions; (c) excitation and charge transfer pathways from both band gap and sub-band gap states E_T contribute to the surface photovoltage signal; and (d) electron transfer into surface states E_S limits the recombination rate at t > 800 s.

and Figure S10). This variation in times may be due to differences in surface states across the series, differences in specific surface areas, or differences in Fermi energies. We hope to gain further insight into these parameters in future investigations.

Much like Ce₂O₂S₂⁵³ Ce₁₀S₁₄O presents interesting optoelectronic properties. In stark contrast with the remaining light lanthanoid oxysulfides, Ce₁₀S₁₄O exhibits a considerably narrower band gap, which endows it with a bright red color (Figure 4a) and no observable charge separation upon illumination (Figure S9). Previous studies on Ce₂O₂S have shown that oxidation can generate homogeneously disperse Ce(IV) ions with trapped electrons, which can lead to valence band \rightarrow excitonic-type level transitions. ^{54,55} However, there is no evidence of the existence of Ce(IV) in Ce₁₀S₁₄O due to the absence of its characteristic XPS and XAS signals (Figures 3 and S6). Ce(III) presents intense orbitally allowed $4f \rightarrow 5d$ transitions in the 650-500 nm range, 54,56 which may explain the lack of photovoltage signal through fast exciton recombination. Further transient absorption and photoluminescence studies may shed light into the distinct optical properties of this oxysulfide.

CONCLUSIONS

 ${\rm Ln_{10}S_{14}O}$ are a series of complex oxysulfides with large unit cells that demonstrate semiconducting properties. Based on diffuse reflectance UV—vis spectroscopy, all ${\rm Ln_{10}S_{14}O}$ studied show band gap energies in the visible region of the electromagnetic spectrum, exhibiting colors from white-yellow for La to bright red for Ce. Furthermore, through Tauc plot and DASF analysis, we determined for the first time that these oxysulfides are direct semiconductors.

Surface photovoltage spectroscopy showed that the majority carriers in $La_{10}S_{14}O$, $Pr_{10}S_{14}O$, $Nd_{10}S_{14}O$, and $Sm_{10}S_{14}O$ are electrons, classifying them as n-type semiconductors. La, Pr, Nd, and Sm oxysulfides exhibit appreciable surface photovoltage signals at energies below their corresponding optical band gaps, which may be rooted in sulfide vacancies and lanthanoid 4f orbitals forming mid-gap donor states. Moreover, photovoltage decay spectroscopy experiments revealed that carrier recombination at long timescales (t > 800 s) is limited by electron transfer into surface states. The observation of long-lived photogenerated charge carriers in lanthanoid oxysulfides may be of interest for their utilization as potential photocatalysts or light absorbers in solar energy conversion applications. On the other hand, the intensely red colored

 $Ce_{10}S_{14}O$ (band gap 2 eV) shows no surface photovoltage, the cause of which is a target of ongoing studies.

EXPERIMENTAL METHODS

Synthesis. All lanthanoid oxysulfides were synthesized through a high-temperature solid-state sulfurization method in a tube furnace, using H₂S (Matheson Tri Gas) as sulfur source and Ar or forming gas (96% Ar, 4% H₂) as carrier gases. La₁₀S₁₄O, Nd₁₀S₁₄O, and Sm₁₀S₁₄O were synthesized starting from their corresponding oxides, Ln₂O₃ (99.5%, Sigma-Aldrich). The synthesis of Pr₁₀S₁₄O comprised a twostep method. First, 1 g of Pr(NO₃)₃·6H₂O (99.9%, Sigma-Aldrich) was dissolved in 20 mL of Nanopure water (18 M Ω resistivity). Amorphous Pr(OH)3 was then precipitated by slow addition of stoichiometric amounts of 1 M NaOH, and the obtained solid was vacuum filtered. The solid was washed with Nanopure water and dried under air. $Ce_{10}S_{14}O$ synthesis used CeO_2 (Sigma-Aldrich) as the precursor and forming gas to perform the reduction of Ce(IV) to Ce(III). In a typical synthesis, 100 mg of the lanthanide precursor is evenly distributed in an alumina boat such that the surface area is maximized, introduced into an open quartz tube and placed in the center of a tube furnace (Lindberg Blue M, Thermo Fisher). The air contained within the tube is removed by application of vacuum for 5 min, followed by back filling with Ar to atmospheric pressure, and opening to a bubbler placed downstream, thus ensuring that the flowing reaction medium is inert. Afterward, the sample is heated to 1100 °C (44 °C/min ramp rate) under 100 sccm of carrier gas. When the target temperature is reached, 10 sccm of H₂S is added to the reaction mixture and sulfurization is carried out for ~1 h (time will depend upon the exact mass of the precursor used). Subsequently, the flow of H₂S is stopped and the sample cooled under the carrier gas flow (50 °C/min ramp rate).

Characterization. Powder X-ray Diffraction (PXRD). Diffractograms from each solid were obtained using a Bruker Eco-Advance diffractometer equipped with a Cu $K\alpha$ source (1.5406 Å). Rietveld refinements were performed using the Topas software (Bruker).

Diffuse Reflectance UV–vis. Sample powders were suspended (20 mg/mL) in isopropanol (IPA) by sonication for at least 20 min and dropcasted onto glass slides. The reflectance spectra of the dry films were measured in a Thermo Fisher Evolution 220 spectrophotometer in which an Al_2O_3 standard (Labsphere) was used for background subtraction

Scanning Electron Microscopy (SEM). Micrographs of different oxysulfides were obtained with a Scios scanning electron microscope (FEI), equipped with an energy dispersive X-ray spectroscope (Oxford Instruments). Due to their large band gaps, samples were sputtered with gold using a Quorum Tech Q150RES sputter coater before imaging. Typically, 5 nm of Au was sputtered onto powders.

Surface Photovoltage Spectroscopy (SPS). Measurements of $Ln_{10}S_{14}O$ particle films were conducted under vacuum (<2 × 10⁻⁴ mbar). A gold Kelvin probe (Delta PHI Besocke) served as the reference electrode. Samples were illuminated with monochromatic light from a 300 W halogen lamp filtered through an Oriel Cornerstone 130 monochromator (0.001-0.86 mW cm⁻²; Newport Corporation, Irvine, CA) in the 3390-40,000 cm⁻¹ regime. Transient surface photovoltage measurements were performed using a 400 nm LED at 12.5 mW cm⁻² that was turned on and off after reaching a steady value. One data point was taken per second. The contact potential difference (CPD) spectra and decay scans were corrected for drift effects by subtracting a fitted logarithmic curve of a dark scan from the light scan. Sample films were deposited on FTO substrates (sonicated twice in acetone, rinsed with Nanopure water, sonicated in Nanopure water, and dried in air at 70 °C before use). Approximately 5 mg of $Ln_{10}S_{14}O$ was dispersed in 500 μL of pure ethanol by sonicating for 30 min. Particle suspension (20 μ L) was dropped on the FTO substrate with a circle mask of 7 mm diameter. Films were allowed to dry in air at room temperature. Additional layers of 20 μL of the particle suspension were applied if the film appeared highly transparent.

X-ray Absorption Spectroscopy (XAS). Ln L-edge X-ray absorption spectroscopy was performed at the Stanford Synchrotron Radiation Lightsource (SSRL, BL 4–3) and analyzed with the Demeter software package (see Supporting Information). S7,58 Samples were loaded under air, into a well equipped with Kapton windows. Measurements were performed in fluorescence mode, using a Lytle detector; appropriate metal reference foils were concomitantly measured in transmission mode for energy calibration. The beamline was equipped with three ionization chambers through which N_2 gas was flown.

X-ray Photoelectron Spectroscopy (XPS). Photoelectron spectroscopy was carried out in a Kratos Supra Axis Spectrometer (Shimadzu corporation) with a monochromatic Al K α source (1486.6 eV). Data was processed with the ESCApe software. Charge correction was applied using adventitious C 1s (284.4 eV) as reference; high-resolution scans were fitted with a static Shirley background function, ⁵⁹ and peaks were modeled using a Gaussian*Lorentzian 0.3 mixture (where 1 is full Lorentzian).

Mott–Schottky Analysis. Electrodes were prepared by dropcasting a suspension of each lanthanoid oxysulfide in isopropanol (20 mg/mL) onto indium tin oxide (ITO)-coated glass slides. Front electrical contacts were made with conductive silver paint, and epoxy resin was used to mask the electrical contact and delimit the electrode area (~1 cm in diameter). Staircase potentio-electrochemical impedance spectroscopy (SPEIS) was performed with a bipotentiostat (Biologic S.A.) with a sinusoidal amplitude of 10 mV in the potential range of –1 to 0 V vs Ag/AgCl, in a 0.1 M Na₂SO₄ electrolyte purged with argon for 10 min, with graphite as a counter electrode.

ASSOCIATED CONTENT

Supporting Information

The Supporting Information is available free of charge at https://pubs.acs.org/doi/10.1021/acs.chemmater.2c01244.

Rietveld refinements; EXAFS fitting parameters; Raman spectra; SEM images; Tauc plot fitting parameters; extended-range DASF analyses fits; and additional SPS data (PDF)

AUTHOR INFORMATION

Corresponding Authors

Frank E. Osterloh – Department of Chemistry, University of California, Davis, California 95616, United States;

o orcid.org/0000-0002-9288-3407; Email: fosterloh@ucdavis.edu

Jesús M. Velázquez – Department of Chemistry, University of California, Davis, California 95616, United States;

orcid.org/0000-0003-2790-0976; Email: jevelazquez@ucdavis.edu

Authors

Brian A. Wuille Bille — Department of Chemistry, University of California, Davis, California 95616, United States;

© orcid.org/0000-0003-2745-2499

Anna C. Kundmann – Department of Chemistry, University of California, Davis, California 95616, United States

Complete contact information is available at: https://pubs.acs.org/10.1021/acs.chemmater.2c01244

Author Contributions

All authors have given approval to the final version of the manuscript.

Notes

The authors declare no competing financial interest.

SAFETY: H_2S is an acutely toxic gas that must be placed in a properly ventilated location with adequate engineering controls. In our setup, the cylinder is located inside a fume

hood, and a detector (Honeywell) is used to alert of any potential leaks. Furthermore, it is advisable to place a suitable scrubber downstream to trap unreacted H_2S (e.g., NaOH + H_2O_2).

ACKNOWLEDGMENTS

J.M.V. thanks the University of California, Davis, for start-up funding. J.M.V. also acknowledges support from the Cottrell Scholars program supported by the Research Corporation for Science Advancement (RCSA 26780), as well as support from the National Science Foundation through the Faculty Early Career Development Program (DMR-2044403) and the Camille Dreyfus Teacher-Scholar Awards Program (TC-22-096-0). Use of the Stanford Synchrotron Radiation Lightsource, SLAC National Accelerator Laboratory, is supported by the U.S. Department of Energy, Office of Science, Office of Basic Energy Sciences under Contract No. DE-AC02-76SF00515. XPS characterization was performed at the Advanced Materials Characterization and Testing Laboratory (AMCaT), funded through the National Science Foundation (DMR-1828238). Part of this study was carried out at the UC Davis Center for Nano and Micro Manufacturing (CNM2). Support for surface photovoltage spectroscopy measurements was provided by the U.S. Department of Energy, Office of Science, Office of Basic Energy Sciences under Award Number DOE-SC0015329.

ABBREVIATIONS USED

DASF, derivation of absorption spectrum fitting; XAS, X-ray absorption spectroscopy; SPS, surface photovoltage spectroscopy; XPS, X-ray photoelectron spectroscopy

REFERENCES

- (1) Haxel, G. B.; Hedrick, J. B.; Orris, G. J. Rare Earth Elements Critical Resources for High Technology https://pubs.usgs.gov/fs/2002/fs087-02 (accessed Dec 10, 2021).
- (2) Bünzli, J.-C. G. Benefiting from the Unique Properties of Lanthanide Ions. Acc. Chem. Res. 2006, 39, 53-61.
- (3) Tricoire, M.; Mahieu, N.; Simler, T.; Nocton, G. Intermediate Valence States in Lanthanide Compounds. *Chem. Eur. J.* **2021**, *27*, 6860–6879.
- (4) Múnera, J. F.; Irusta, S.; Cornaglia, L. M.; Lombardo, E. A.; Vargas Cesar, D.; Schmal, M. Kinetics and Reaction Pathway of the CO2 Reforming of Methane on Rh Supported on Lanthanum-Based Solid. *J. Catal.* **2007**, *245*, 25–34.
- (5) Call, F.; Roeb, M.; Schmu, M.; Sattler, C.; Pitz-paal, R. Ceria Doped with Zirconium and Lanthanide Oxides to Enhance Solar Thermochemical Production of Fuels. *J. Phys. Chem. C* **2015**, *119*, 6929–6938.
- (6) Ranjit, K. T.; Bossmann, S. H.; Braun, A. M.; et al. Lanthanide Oxide-Doped Titanium Dioxide Photocatalysts: Novel Photocatalysts for the Enhanced Degradation of p -Chlorophenoxyacetic Acid. *Environ. Sci. Technol.* **2001**, *35*, 1544–1549.
- (7) Golubkov, A. V.; Kazanin, M. M.; Kaminskii, V. V.; Sokolov, V. V.; et al. Thermoelectric Properties of SmS_x (x = 0.8–1.5). *Inorg. Mater.* **2003**, 39, 1251–1256.
- (8) Jundale, S. B.; Lokhande, C. D. (Photo) Electrochemical Studies on p-Sm₂S₃ Films. *Sol. Energy Mater. Sol. Cells* **1992**, 28, 151–157.
- (9) Maestro, P.; Huguenin, D. Industrial Applications of Rare Earths: Which Way for the End of the Century. *J. Alloys Compd.* **1995**, 225, 520–528.
- (10) Tomczak, J. M.; Pourovskii, L. V.; Vaugier, L.; Georges, A.; Biermann, S. Rare-Earth vs. Heavy Metal Pigments and Their Colors from First Principles. *Proc. Natl. Acad. Sci. U.S.A.* **2013**, *110*, 904–907.

- (11) Schleid, T.; Lissner, F. $\rm M_{10}S_{14}O$ -Type Oxysulphides (M = La, Ce, Pr, Nd, Sm) as an "Oxygen Trap" in Oxidation Reactions of Reduced Lanthanide Chlorides with Sulphur. *J. Less-Common Met.* **1991**, 175, 309–319.
- (12) Liu, Y.; Jing, X.; Wang, P.; Yin, T.; Ji, D.; Zhang, M. Rapid Production of $Ln_2O_2S:Eu^{3+}/Tb^{3+}$ (Ln = Sm, La, Gd, and Y) Phosphors by Molten Salt Electrolysis. *ACS Appl. Energy Mater.* **2018**, *1*, 1191–1199.
- (13) Lin, S. L.; Liu, T. Y.; Lo, C. L.; Wang, B. S.; Lee, Y. J.; Lin, K. Y.; Chang, C. A. Synthesis, Surface Modification, and Photophysical Studies of Ln₂O₂S:Ln'³⁺ (Ln = Gd, Tb, Eu; Ln' = Tb and/or Eu) Nanoparticles for Luminescence Bioimaging. *J. Lumin.* **2016**, *175*, 165–175.
- (14) Valsamakis, I.; Flytzani-Stephanopoulos, M. Sulfur-Tolerant Lanthanide Oxysulfide Catalysts for the High-Temperature Water-Gas Shift Reaction. *Appl. Catal. B* **2011**, *106*, 255–263.
- (15) Tan, S.; Paglieri, S. N.; Li, D. Nano-Scale Sulfur-Tolerant Lanthanide Oxysulfide/Oxysulfate Catalysts for Water-Gas-Shift Reaction in a Novel Reactor Configuration. *Catal. Commun.* **2016**, 73, 16–21.
- (16) Bludau, W.; Wichelhaus, W. Photoluminescence of Doped La₁₀S₁₄O. *J. Appl. Phys.* **1981**, *52*, 2750–2755.
- (17) Ikeue, K.; Ando, S.; Mitsuyama, T.; Ohta, Y.; Arayama, K.; Tsutsumi, A.; Machida, M. Photocatalytic Property and Electronic Structure of Lanthanide-Based Oxysulfides. *Top. Catal.* **2008**, *47*, 175–180
- (18) Schleid, T.; Weber, F. A. Crystal Structure of Dekagadolinium-(III) Oxide Tetradekasulfide, $Gd_{10}OS_{14}$. Z. Kristallogr. New Cryst. Struct. 1998, 213, 32.
- (19) Besançon, P.; Carré, D.; Laruelle, P. Mécanisme de La Solution Solide Des Oxysulfures de Terres Rares $L_{10}S_{15-x}O_X$. Acta Crystallogr., Sect. B: Struct. Crystallogr. Cryst. Chem. 1973, 29, 1064–1066.
- (20) Besançon, P. Teneur En Oxygéne et Formule Exacte d'une Famille de Composés Habituellement Appelés "Variété β " Ou "Phase Complexe" Des Sulfures de Terres Rares. *J. Solid State Chem.* **1973**, 7, 232–240.
- (21) Vaughan, C. M.; White, W. B. Role of Oxygen in Rare-Earth Chalcogenide Semiconductors. *MRS Online Proc. Libr.* **1987**, 97, 397–402.
- (22) Knight, D. S.; White, W. B. Raman Line Widths in Rare-Earth Sesquisulfides Solid Solutions. *J. Am. Ceram. Soc.* **1996**, *79*, 1394–1396.
- (23) Knight, D. S.; White, W. B. Raman Spectroscopic Study of the Rare Earth Sesquisulfides. *Spectrochim. Acta, Part A* **1990**, 46, 381–387.
- (24) Asakura, H.; Shishido, T.; Fuchi, S.; Teramura, K.; Tanaka, T. Local Structure of Pr, Nd, and Sm Complex Oxides and Their X-Ray Absorption near Edge Structure Spectra. *J. Phys. Chem. C* **2014**, *118*, 20881–20888.
- (25) Löble, M. W.; Keith, J. M.; Altman, A. B.; Stieber, S. C. E.; Batista, E. R.; Boland, K. S.; Conradson, S. D.; Clark, D. L.; Lezama Pacheco, J.; Kozimor, S. A.; Martin, R. L.; Minasian, S. G.; Olson, A. C.; Scott, B. L.; Shuh, D. K.; Tyliszczak, T.; Wilkerson, M. P.; Zehnder, R. A. Covalency in Lanthanides. An X-Ray Absorption Spectroscopy and Density Functional Theory Study of $LnCl_6^{x-}$ (x=3, 2). *J. Am. Chem. Soc.* **2015**, 137, 2506–2523.
- (26) Gompa, T. P.; Ramanathan, A.; Rice, N. T.; La Pierre, H. S. The Chemical and Physical Properties of Tetravalent Lanthanides: Pr, Nd, Tb, and Dy. *Dalton Trans.* **2020**, *49*, 15945–15987.
- (27) Kvashnina, K. O.; Butorin, S. M.; Glatzel, P. Direct Study of the F-Electron Configuration in Lanthanide Systems. *J. Anal. At. Spectrom.* **2011**, *26*, 1265–1272.
- (28) Jørgensen, C. K.; Berthou, H. Split Photo-Electron Signals from the Unique Closed-Shell Cation Lanthanum(III). *Chem. Phys. Lett.* **1972**, *13*, 186–189.
- (29) Signorelli, A. J.; Hayes, R. G. X-Ray Photoelectron Spectroscopy of Various Core Levels of Lanthanide Ions: The Roles of Monopole Excitation and Electrostatic Coupling. *Phys. Rev. B: Condens. Matter Mater. Phys.* 1973, 8, 81–86.

- (30) Berthou, H.; Jorgensen, C. K.; Bonnelle, C. Influence of The Ligands on 3d Photoelectron Spectra of the First Four Lanthanides. *Chem. Phys. Lett.* **1976**, 38, 199–206.
- (31) Burroughs, P.; Hamnett, A.; Orchard, A. F.; Thornton, G. Satellite Structure in the X-Ray Photoelectron Spectra of Some Binary and Mixed Oxides of Lanthanum and Cerium. *J. Chem. Soc., Dalton Trans.* 1976, 1686–1698.
- (32) Tauc, J.; Grigorovici, R.; Vancu, A. Optical Properties and Electronic Structure of Amorphous Germanium. *Phys. Status Solidi B* **1966**, *15*, 627–637.
- (33) Kubelka, P.; Munk, F. Ein Beitrag Zur Optik Der Farbanstriche. Z. Tech. Phys. 1931, 12, 593–601.
- (34) Makuła, P.; Pacia, M.; Macyk, W. How To Correctly Determine the Band Gap Energy of Modified Semiconductor Photocatalysts Based on UV-Vis Spectra. *J. Phys. Chem. Lett.* **2018**, *9*, 6814–6817.
- (35) Souri, D.; Tahan, Z. E. A New Method for the Determination of Optical Band Gap and the Nature of Optical Transitions in Semiconductors. *Appl. Phys. B: Lasers Opt.* **2015**, *119*, 273–279.
- (36) Runowski, M.; Stopikowska, N.; Lis, S. UV-Vis-NIR Absorption Spectra of Lanthanide Oxides and Fluorides. *Dalton Trans.* **2020**, 49, 2129–2137.
- (37) Donchev, V.; Kirilov, K.; Ivanov, T.; Germanova, K. Surface Photovoltage Phase Spectroscopy a Handy Tool for Characterisation of Bulk Semiconductors and Nanostructures. *Mater. Sci. Eng., B* **2006**, 129, 186–192.
- (38) Kronik, L.; Shapira, Y. Surface Photovoltage Spectroscopy of Semiconductor Structures: At the Crossroads of Physics, Chemistry and Electrical Engineering. *Surf. Interface Anal.* **2001**, *31*, 954–965.
- (39) Melo, M. A.; Osterloh, F. E. Defect States Control Effective Band Gap and Photochemistry of Graphene Quantum Dots. ACS Appl. Mater. Interfaces 2018, 10, 27195–27204.
- (40) Wu, P.; Wang, J.; Zhao, J.; Guo, L.; Osterloh, F. E. Structure Defects in G-C₃N₄ Limit Visible Light Driven Hydrogen Evolution and Photovoltage. *J. Mater. Chem. A* **2014**, *2*, 20338–20344.
- (41) Ma, X.; Wu, Z.; Roberts, E. J.; Han, R.; Rao, G.; Zhao, Z.; Lamoth, M.; Cui, X.; Britt, R. D.; Osterloh, F. E. Surface Photovoltage Spectroscopy Observes Sub-Band-Gap Defects in Hydrothermally Synthesized SrTiO₃ Nanocrystals. *J. Phys. Chem. C* **2019**, *123*, 25081–25090.
- (42) Zhuang, G.; Yan, J.; Wen, Y.; Zhuang, Z.; Yu, Y. Two-Dimensional Transition Metal Oxides and Chalcogenides for Advanced Photocatalysis: Progress, Challenges, and Opportunities. *Solar RRL* **2021**, *5*, No. 2000403.
- (43) Shin, D.; Saparov, B.; Mitzi, D. B. Defect Engineering in Multinary Earth-Abundant Chalcogenide Photovoltaic Materials. *Adv. Energy Mater.* **2017**, *7*, No. 1602366.
- (44) Colombara, D.; Elanzeery, H.; Nicoara, N.; Sharma, D.; Claro, M.; Schwarz, T.; Koprek, A.; Wolter, M. H.; Melchiorre, M.; Sood, M.; Valle, N.; Bondarchuk, O.; Babbe, F.; Spindler, C.; Cojocaru-Miredin, O.; Raabe, D.; Dale, P. J.; Sadewasser, S.; Siebentritt, S. Chemical Instability at Chalcogenide Surfaces Impacts Chalcopyrite Devices Well beyond the Surface. *Nat. Commun.* 2020, 11, No. 3634.
- (45) Govindaraju, G. V.; Morbec, J. M.; Galli, G. A.; Choi, K. S. Experimental and Computational Investigation of Lanthanide Ion Doping on BiVO₄ Photoanodes for Solar Water Splitting. *J. Phys. Chem. C* **2018**, *122*, 19416–19424.
- (46) Mikami, M.; Nakamura, S. Electronic Structure of Rare-Earth Sesquioxides and Oxysulfides. *J. Alloys Compd.* **2006**, 408–412, 687–692.
- (47) Dittrich, T. Surface Photovoltage Analysis of Photoactive Materials; World Scientific Publishing Europe Ltd.: London, 1999; p 188.
- (48) Kronik, L.; Shapira, Y. Surface Photovoltage Phenomena: Theory, Experiment, and Applications. *Surf. Sci. Rep.* **1999**, *37*, 1–206.
- (49) Mora-Seró, I.; Dittrich, T.; Garcia-Belmonte, G.; Bisquert, J. Determination of Spatial Charge Separation of Diffusing Electrons by Transient Photovoltage Measurements. *J. Appl. Phys.* **2006**, *100* (10), 103705.

- (50) Peter, L. M.; Li, J.; Peat, R. Surface Recombination at Semiconductor Electrodes. Part I. Transient and Steady-State Photocurrents. J. Electroanal. Chem. Interfacial Electrochem. 1984, 165, 29–40.
- (51) Li, K.; Miao, B.; Fa, W.; Chen, R.; Jin, J.; Bevan, K. H.; Wang, D. Evolution of Surface Oxidation on Ta_3N_5 as Probed by a Photoelectrochemical Method. *ACS Appl. Mater. Interfaces* **2021**, *13*, 17420–17428.
- (52) Salvador, P.; Gutiérrez, C. Analysis of the Transient Photocurrent-Time Behaviour of a Sintered n-SrTiO₃ Electrode in Water Photoelectrolysis. *J. Electroanal. Chem. Interfacial Electrochem.* 1984, 160, 117–130.
- (53) Larquet, C.; Nguyen, A. M.; Glais, E.; Paulatto, L.; Sassoye, C.; Selmane, M.; Lecante, P.; Maheu, C.; Geantet, C.; Cardenas, L.; Chanéac, C.; Gauzzi, A.; Sanchez, C.; Carenco, S. Band Gap Engineering from Cation Balance: The Case of Lanthanide Oxysulfide Nanoparticles. *Chem. Mater.* **2019**, *31*, 5014–5023.
- (54) Sourisseau, C.; Cavagnat, R.; Mauricot, R.; Boucher, F.; Evain, M. Structure and Bondings in Cerium Oxysulfide Compounds I Electronic, Infrared and Resonance Raman Spectra of Ce_{2.0}O_{2.5}S. *J. Raman Spectrosc.* **1997**, 28, 965–971.
- (55) Larquet, C.; Nguyen, A. M.; Ávila-Gutiérrez, M.; Tinat, L.; Lassalle-Kaiser, B.; Gallet, J. J.; Bournel, F.; Gauzzi, A.; Sanchez, C.; Carenco, S. Synthesis of Ce₂O₂S and Gd_{2(1-y)}Ce_{2y}O₂S Nanoparticles and Reactivity from in Situ X-Ray Absorption Spectroscopy and X-Ray Photoelectron Spectroscopy. *Inorg. Chem.* **2017**, *56*, 14227–14236.
- (56) Pan, G.; Bai, X.; Yang, D.; Chen, X.; Jing, P.; Qu, S.; Zhang, L.; Zhou, D.; Zhu, J.; Xu, W.; Dong, B.; Song, H. Doping Lanthanide into Perovskite Nanocrystals: Highly Improved and Expanded Optical Properties. *Nano Lett.* **2017**, *17*, 8005–8011.
- (57) Ravel, B.; Newville, M. ATHENA, ARTEMIS, HEPHAESTUS: Data Analysis for X-Ray Absorption Spectroscopy Using IFEFFIT. *J. Synchrotron Radiat.* **2005**, *12*, 537–541.
- (58) Newville, M. IFEFFIT: Interactive XAFS Analysis and FEFF Fitting. J. Synchrotron Radiat. 2001, 8, 322–324.
- (59) Engelhard, M. H.; Baer, D. R.; Herrera-gomez, A.; Herrera-Gomez, A.; Sherwood, P. M. A. Introductory Guide to Backgrounds in XPS Spectra and Their Impact on Determining Peak Intensities. *J. Vac. Sci. Technol. A* **2020**, *38*, No. 063203.